

Decentralized Geometric Control for Cable-Suspended Payload Transport with Adaptive Mass Estimation

Author Names Omitted for Review

Affiliation Omitted for Review

Abstract—Cooperative aerial transport—where multiple quadrotors jointly carry a payload via cable suspensions—promises extended payload capacity and fault tolerance, but demands controllers that respect nonlinear manifold geometry, operate without centralized coordination, and systematically enforce safety constraints. We present GPAC (Geometric Position and Attitude Control), a four-layer hierarchical architecture enabling N quadrotors to transport a cable-suspended payload with zero inter-agent state exchange. The key insight is *implicit coordination*: each drone independently estimates its payload mass share $\hat{\theta}_i \rightarrow m_L/N$ from local cable measurements using concurrent learning, causing the combined forces to automatically converge to the correct total $\sum_i F_i \rightarrow m_L \cdot u$ —without knowledge of N , m_L , or any peer’s state. Operating directly on $\text{SE}(3) \times (\mathbb{S}^2)^N$ without linearization, GPAC integrates: (i) geometric position/attitude control with anti-swing regulation, (ii) an extended state observer for wind rejection, (iii) concurrent learning mass estimation converging in ~ 8 s without persistent excitation, and (iv) a control barrier function (CBF) safety filter enforcing cable tautness, angle limits, tilt bounds, and collision avoidance with input-to-state safety (ISSf) guarantees. We prove that CBF-induced modifications preserve almost-global exponential attitude stability on $\text{SO}(3)$. Validated in high-fidelity Drake simulation with flexible bead-chain cables, 15-state ESKF sensor fusion, and Dryden turbulence, GPAC achieves 23.7 ± 1.5 cm tracking RMSE (3.3% of workspace diagonal) at under 1 MFLOP/s per agent—demonstrating that geometric rigor, full decentralization, and certified safety can coexist.

Index Terms—Cooperative aerial transport, geometric control, decentralized systems, adaptive estimation, control barrier functions, multi-UAV systems.

I. INTRODUCTION

Cooperative aerial transport—in which multiple unmanned aerial vehicles (UAVs) jointly manipulate a common payload via cable suspensions—extends payload capacity, workspace, and fault tolerance beyond the limits of any single platform. Applications span construction logistics, emergency supply delivery, and assembly of large-scale structures in environments inaccessible to ground vehicles. Such systems are inherently safety-critical: cable slack, excessive swing, vehicle tilt, inter-agent collisions, and environmental disturbances can each independently cause loss of controllability or payload instability. Realizing the potential of N cooperative quadrotors therefore demands controllers that simultaneously respect the nonlinear manifold structure of the configuration space, operate without centralized coordination, and systematically mitigate these dominant failure modes.

A. Related Work and Open Gaps

Geometric control. Lee, Sreenath, and Kumar [1], [2] formulated cable-suspended transport on $\text{SE}(3) \times (\mathbb{S}^2)^N$, with attitude on $\text{SO}(3)$ and cable direction $q_i \in \mathbb{S}^2$, yielding almost-global stability guarantees free of Euler-angle singularities. Extensions [3], [4] added anti-swing control via $\Psi_q = 1 - q_d \cdot q$. Sharma and Sundaram [5] proposed a tractable geometric controller for multi-UAV payload transfer that does not require link information, and Sun et al. [6] recently demonstrated agile cooperative cable manipulation with online kinodynamic planning. However, these controllers assume centralized state knowledge or require full-state payload feedback: every drone must know N , m_L , or all peers’ states—impractical when team size may change or communication cannot be guaranteed. A comprehensive survey of cable-suspended aerial transport is provided in [7].

Decentralized and adaptive methods. Consensus-based formation controllers [8] and distributed optimization rely on linearized dynamics and Euclidean error metrics that forfeit global stability during large-angle maneuvers—precisely when guarantees are most needed. Wang et al. [9] proposed Auto-Multilift, a distributed learning framework that tunes MPC cost functions online for cooperative load transport, but it relies on optimization-based MPC rather than geometric control and does not provide Lyapunov stability certificates. The concurrent learning paradigm [10], [11], enabling convergence without persistent excitation (PE) by exploiting stored data, is particularly relevant because cooperative hover provides insufficient excitation for classical adaptive laws; yet existing applications remain confined to centralized single-vehicle settings.

Safety-critical control. Cable-suspended transport imposes real-time state constraints: cables must remain taut, cable angles bounded, swing rates limited, and collisions prevented. Control Barrier Functions (CBFs) [12], [13] enforce such constraints via online QPs that minimally modify a nominal controller. Yang and Xie [14] recently combined CBFs with disturbance estimators for single-quadrotor cable-suspended payload safety, demonstrating that disturbance-observer CBFs reduce conservatism under model uncertainty. However, integrating CBFs with geometric controllers on nonlinear manifolds while preserving Lyapunov certificates remains open, particularly in decentralized multi-agent settings where coupled constraints and attitude stability certificates must coexist.

Simulation realism. Most geometric transport results assume

rigid cables and perfect state feedback. Real cables exhibit compliance, wave propagation, and slack-to-taut transitions that significantly affect system behavior [15]. Onboard estimation must fuse noisy IMU, GPS, and barometer via nonlinear filters [16], while wind introduces unmodeled forces [17]. The robustness of geometric cooperative controllers to these conditions remains largely uncharacterized.

B. Design Philosophy: Hazard-Oriented Decomposition

A central principle in safety-critical system engineering is the early identification and systematic mitigation of dominant hazards [18]. Rather than designing a monolithic controller and verifying safety post-hoc, each GPAC layer directly addresses a specific cooperative transport hazard: anti-swing regulation stabilizes pendular modes, adaptive estimation mitigates load uncertainty, the ESO compensates environmental disturbances, and the CBF layer enforces physical constraints as a runtime supervisor. The hierarchical multi-rate structure with deliberate timescale separation limits fault propagation between layers; the fully decentralized implementation eliminates single points of failure [19]. Table VI in Section VI validates this mapping with measured performance data.

C. Contributions

The GPAC architecture decomposes the cooperative transport problem into N identical single-agent subproblems via a key insight: each drone independently estimates its payload mass share $\hat{\theta}_i \approx m_L/N$ from local cable measurements, and the combined forces automatically sum to the correct total:

$$\sum_{i=1}^N F_i = \sum_{i=1}^N \hat{\theta}_i \cdot u \longrightarrow m_L \cdot u, \quad (1)$$

where $u := g e_3 + \ddot{p}_L^d$ is the common payload acceleration demand (gravity plus desired payload acceleration), which every agent computes identically from the shared reference trajectory. This implicit coordination property—which does not hold for linearized or impedance-based approaches—eliminates the need for a centralized coordinator, payload or cable state exchange, consensus protocols, or knowledge of N and m_L . The only inter-agent information is a low-rate GPS position broadcast (10 Hz) used for collision avoidance. The specific contributions are:

- 1) **Decentralized geometric control on $\text{SE}(3) \times (\mathbb{S}^2)^N$.** To our knowledge, the first decentralized controller for multi-UAV cable transport that operates directly on the nonlinear manifold without linearization. Each agent's policy depends only on its own state and local cable measurements; the only shared information is a reference trajectory (broadcast before flight) and neighbor GPS positions (10 Hz, for collision avoidance only). No payload state, cable state, or adaptive parameter is exchanged.
- 2) **Concurrent learning adaptive estimation without PE.** A decentralized adaptive law in which each drone estimates $\hat{\theta}_i \rightarrow m_L/N$ from local cable tension and direction, with exponential convergence guaranteed by a rank-maximizing

history buffer—even during near-static hover where classical adaptive laws fail.

- 3) **CBF safety filter with formal geometric compatibility.** A modular safety layer enforcing cable tautness, angle, tilt, swing rate, and collision constraints with input-to-state safety (ISSf) guarantees. Theorem 1 proves that the CBF-induced force modifications preserve the almost-global exponential stability of the geometric attitude controller on $\text{SO}(3)$.
- 4) **Sensor-realistic validation with flexible cable dynamics.** High-fidelity Drake-based simulation with bead-chain cables (capturing slack-to-taut transitions and wave propagation), a 15-state ESKF fusing noisy IMU/GPS/barometer, and Dryden wind turbulence, achieving 23.7 ± 1.5 cm payload tracking RMSE over a 6×3 m workspace (3.3% of workspace diagonal) at under 1 MFLOP/s per agent.

These contributions demonstrate that geometric rigor, operational decentralization, and safety guarantees can coexist in a single architecture. The remainder of this paper presents the system model (Section II), control architecture (Section III), adaptive estimation (Section IV), CBF safety filter (Section V), simulation results (Section VI), and conclusion (Section VII).

II. SYSTEM MODELING

The world frame \mathcal{W} has e_3 aligned upward. Rotations lie in $\text{SO}(3)$; the hat map $(\cdot)^\wedge : \mathbb{R}^3 \rightarrow \mathfrak{so}(3)$ satisfies $\hat{v}w = v \times w$. Cable directions $q_i \in \mathbb{S}^2$ have tangent-space projection $P(q) = I_3 - qq^\top$. The full system evolves on

$$\mathcal{Q} = \underbrace{\text{SE}(3)}_{\text{payload}} \times \prod_{i=1}^N \underbrace{\text{SE}(3) \times \mathbb{S}^2}_{\text{drone } i + \text{cable}}, \quad \dim(\mathcal{Q}) = 6 + 8N. \quad (2)$$

The singularity-free geometric error functions are:

$$e_{R_i} = \frac{1}{2}(R_{d_i}^\top R_i - R_i^\top R_{d_i})^\vee, \quad (3)$$

$$\Psi_{q_i} = 1 - q_{d_i} \cdot q_i \in [0, 2], \quad (4)$$

$$e_{q_i} = P(q_i) q_{d_i} \in T_{q_i} \mathbb{S}^2, \quad (5)$$

where e_{q_i} is the negative gradient of Ψ_{q_i} restricted to $T_{q_i} \mathbb{S}^2$.

A. Quadrotor and Payload Dynamics

Each of N identical quadrotors (mass m_Q , body-frame inertia J) obeys

$$m_Q \ddot{p}_i = m_Q g e_3 + f_i R_i e_3 + F_i^{\text{cable}} + F_i^{\text{wind}}, \quad (6)$$

$$J \dot{\Omega}_i = -\Omega_i \times J \Omega_i + \tau_i + \tau_i^{\text{ext}}, \quad (7)$$

with kinematics $\dot{R}_i = R_i \hat{\Omega}_i$, where f_i is the scalar thrust magnitude, τ_i is the body-frame control torque, F_i^{cable} is the cable tension force, and F_i^{wind} is the aerodynamic disturbance. Gravity acts as $-g e_3$ with the thrust $f_i R_i e_3$ directed along the body z -axis. The payload (mass m_L , position p_L) satisfies

$$m_L \ddot{p}_L = -m_L g e_3 + \sum_{i=1}^N F_i^L + F^{\text{contact}} + F_L^{\text{wind}}, \quad (8)$$

where F_i^L is the cable force from the i -th rope at the payload attachment point, and F^{contact} denotes the ground normal and Coulomb friction forces.

The cable direction $q_i \in \mathbb{S}^2$ from the payload toward the quadrotor evolves as $\dot{q}_i = \omega_{q_i} \times q_i$ with $\omega_{q_i} \in T_{q_i} \mathbb{S}^2$. Under the constraint $p_i = p_L + R_L \rho_i^L + L_i q_i$ (where ρ_i^L is the attachment offset in the payload body frame), the swing dynamics on \mathbb{S}^2 are governed by the projected quadrotor acceleration and gravitational restoring torque.

B. Bead-Chain Cable Model

Each cable is discretized as n_b point-mass beads connected by $n_b + 1$ tension-only spring-damper segments. Let b_0 denote the quadrotor attachment, b_1, \dots, b_{n_b} the bead positions, and b_{n_b+1} the payload attachment. Each segment has rest length $L_0 = L_{\text{rest}}/(n_b + 1)$, stretch $\Delta_j = \|b_{j-1} - b_j\| - L_0$, and unit direction $\hat{e}_j = (b_{j-1} - b_j)/\|b_{j-1} - b_j\|$. The tension-only force law is

$$T_j = \begin{cases} k_s \Delta_j + c_s [\dot{\Delta}_j]^+, & \Delta_j > 0, \\ 0, & \Delta_j \leq 0, \end{cases} \quad (9)$$

where $[\cdot]^+ = \max(\cdot, 0)$ restricts damping to the stretching phase. The segment stiffness is derived from a maximum-stretch design criterion ($\epsilon_{\max} = 15\%$):

$$k_s = \frac{F_{\text{load}}}{L_{\text{rest}} \epsilon_{\max}} \cdot (n_b + 1), \quad c_s = c_{\text{ref}} \sqrt{k_s/k_{\text{ref}}}, \quad (10)$$

with $F_{\text{load}} = m_L g / N$ and reference values $k_{\text{ref}} = 300 \text{ N/m}$, $c_{\text{ref}} = 15 \text{ N}\cdot\text{s/m}$. Each bead (mass $m_b = m_{\text{rope}}/n_b$, with $m_{\text{rope}} = 0.2 \text{ kg}$) obeys $m_b \ddot{b}_j = F_j - F_{j+1} - m_b g e_3$. This model naturally captures wave propagation ($\sim \sqrt{k_s L_0}/m_b$), distributed inertia, and the impulsive loading during slack-to-taut transitions absent from rigid-link models. Rope rest lengths are sampled from $L_{\text{rest},i} \sim \mathcal{N}(\bar{L}_i, \sigma_{L,i}^2)$ to model manufacturing uncertainty, yielding up to 19% asymmetry in the simulation.

C. Sensor Models and Wind Disturbance

Each quadrotor carries an onboard sensor suite. The *IMU* (200 Hz) provides body-frame specific force $\tilde{a}_i = R_i^\top (\ddot{p}_i + g e_3) + b_{a,i} + n_{a,i}$ and angular velocity $\tilde{\omega}_i = \Omega_i + b_{g,i} + n_{g,i}$ with noise densities $\sigma_a = 0.004 \text{ m/s}^2/\sqrt{\text{Hz}}$, $\sigma_g = 5 \times 10^{-4} \text{ rad/s}/\sqrt{\text{Hz}}$, and Gauss-Markov biases ($b = -b/\tau + \eta$, $\tau = 3600 \text{ s}$). The *GPS receiver* (10 Hz) provides position with $\sigma_{xy} = 0.02 \text{ m}$, $\sigma_z = 0.05 \text{ m}$, and configurable dropout probability. The *barometric altimeter* (25 Hz) has a three-component noise model: white noise ($\sigma_w = 0.3 \text{ m}$), correlated noise ($\tau_c = 5 \text{ s}$), and slow bias drift (0.002 m/s), with 0.1 m quantization. Cable tension T_i is measured via a load cell ($\sigma_T = 0.5 \text{ N}$) and cable direction q_i via a 2-axis encoder ($\sigma_q = 0.02 \text{ rad}$).

Wind follows the Dryden turbulence spectrum (MIL-F-8785C) [17] with forming filter $H_\alpha(s) = \sigma_\alpha \sqrt{2V/L_\alpha}/(s + V/L_\alpha)$, turbulence intensities $\sigma_u = \sigma_v = 0.5 \text{ m/s}$, $\sigma_w = 0.25 \text{ m/s}$, and altitude-dependent scaling $\sigma_\alpha(h) \propto (h/h_{\text{ref}})^{1/6}$. Spatial correlation between agents decays as $\rho(p_i, p_j) = \exp(-\|p_i - p_j\|/\ell_c)$ with $\ell_c = 10 \text{ m}$, ensuring that closely spaced drones experience similar wind fields. Table I collects all key parameters.

TABLE I
KEY SYSTEM PARAMETERS

Parameter	Symbol	Value
Quadrotor mass / count	m_Q / N	1.5 kg / 3
Payload mass / radius	m_L / r_L	3.0 kg / 0.15 m
Formation radius	r_f	0.6 m
Beads per cable	n_b	8
Rope mass / max stretch	$m_{\text{rope}} / \epsilon_{\max}$	0.2 kg / 15%
IMU rate / noise	$f_{\text{IMU}} / \sigma_a$	200 Hz / 0.004 m/s ² /sqrt(Hz)
GPS rate / noise	$f_{\text{GPS}} / \sigma_{xy}$	10 Hz / 0.02 m
Baro rate / noise	$f_{\text{baro}} / \sigma_w$	25 Hz / 0.3 m
Wind intensity	$\sigma_u, \sigma_v / \sigma_w$	0.5 / 0.25 m/s
Simulation step	Δt_{sim}	0.2 ms

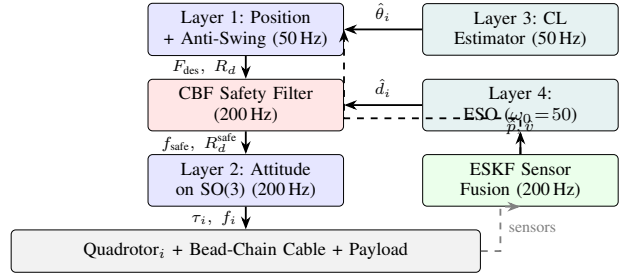


Fig. 1. GPAC per-agent architecture. Blue: control cascade. Red: CBF safety overlay. Teal: estimation. Green: sensor fusion. Each agent executes this pipeline independently; no payload, cable, or estimator states are exchanged (only neighbor GPS positions for collision avoidance).

III. GPAC CONTROL ARCHITECTURE

The GPAC framework is a four-layer hierarchical controller that assigns each physical degree of freedom to a control layer operating at a progressively higher bandwidth (Fig. 1). Each agent i receives only: (i) a shared reference trajectory $p_d(t)$ (broadcast before flight), (ii) its own IMU/GPS/barometer measurements, and (iii) local cable tension T_i and direction q_i . For the collision avoidance barrier, neighbor positions are obtained via GPS broadcast at 10 Hz. No payload state, no other agent's cable state, and no centralized coordinator are required.

Remark 1 (Per-agent sensing and communication). *Each drone measures: IMU (200 Hz), GPS (10 Hz), barometer (25 Hz), cable tension T_i via load cell ($\sigma_T = 0.5 \text{ N}$), cable direction q_i via 2-axis encoder ($\sigma_q = 0.02 \text{ rad}$).* Communication is limited to: (d) a shared precomputed trajectory $p_d(t)$, and (e) neighbor GPS positions (10 Hz) for collision avoidance only. No payload-mounted sensors, no centralized estimator, and no cable state or adaptive parameter exchange are needed.

A. Layer 1: Position Tracking and Anti-Swing Control

The outermost layer (~50 Hz) computes a desired thrust vector:

$$F_{\text{des},i} = F_{\text{fb},i} + F_{\text{ff},i} + F_{\text{cable},i} + F_{\text{swing},i} + F_{\text{eso},i}, \quad (11)$$

combining five physically motivated components. The PID trajectory tracking feedback (with per-axis anti-windup at $|e_{I,k}| \leq 2.0$) is

$$F_{fb,i} = -K_p e_{p_i} - K_d e_{v_i} - K_i e_{I_i}, \quad (12)$$

with $K_p = \text{diag}(6, 6, 8)$, $K_d = \text{diag}(8, 8, 10)$, $K_i = \text{diag}(0.1, 0.1, 0.2)$. The feedforward term compensates gravity and the nominal trajectory: $F_{ff,i} = m_Q(a_{d_i} + g e_3)$.

Cable tension compensation prevents the position controller from treating cable force as a disturbance:

$$F_{\text{cable},i} = \kappa_T(t) T_i q_i, \quad \kappa_T(t) = \min(1, (t - t_{\text{taut},i})/\Delta_{\text{ramp}}), \quad (13)$$

where $t_{\text{taut},i}$ is the time cable i first reaches $T_i \geq 1.0 \text{ N}$ and $\Delta_{\text{ramp}} = 2 \text{ s}$. The gain ramp gradually enables tension compensation using only the *measured* cable force—no knowledge of m_L or N is required. This prevents impulsive loading during the slack-to-taut transition while remaining fully consistent with the decentralized estimation pipeline.

Anti-swing control suppresses pendular oscillations intrinsically on \mathbb{S}^2 [3]:

$$F_{\text{swing},i} = k_q e_{q_i} - k_\omega \omega_{q_i}, \quad (14)$$

with $k_q = 4.0$, $k_\omega = 2.0$. Here e_{q_i} (5) steers $q_i \rightarrow q_{d_i}$ along the geodesic and $\omega_{q_i} \in T_{q_i} \mathbb{S}^2$ is the cable angular velocity. Together, these terms reduce Ψ_{q_i} monotonically absent external perturbation. The ESO disturbance estimate (Layer 4) is fed forward as $F_{\text{eso},i} = m_Q \hat{d}_i$.

The desired rotation $R_{d_i} \in \text{SO}(3)$ is extracted from $F_{\text{des},i}$ by aligning the body z -axis with the thrust direction [1]:

$$b_{3c} = \frac{F_{\text{des},i}}{\|F_{\text{des},i}\|}, \quad b_{2c} = \frac{b_{3c} \times b_{1d}}{\|b_{3c} \times b_{1d}\|}, \quad b_{1c} = b_{2c} \times b_{3c}, \quad (15)$$

with $b_{1d} = [\cos \psi_d, \sin \psi_d, 0]^\top$ setting the desired heading.

B. Layer 2: Geometric Attitude Control on $\text{SO}(3)$

The inner attitude loop (200 Hz) applies the geometric tracking controller [1]:

$$\tau_i = -k_R e_{R_i} - k_\Omega e_{\Omega_i} + \Omega_i \times J \Omega_i, \quad (16)$$

with $k_R = 8.0$, $k_\Omega = 1.5$, and angular velocity error $e_{\Omega_i} = \Omega_i - R_i^\top R_{d_i} \Omega_{d_i}$. The first two terms provide proportional-derivative control on $\text{SO}(3)$; the third compensates gyroscopic coupling. The feedforward terms $\widehat{\Omega}_i R_i^\top R_{d_i} \Omega_{d_i} - R_i^\top R_{d_i} \dot{\Omega}_{d_i}$ are omitted under the simplification $\Omega_{d_i} \approx 0$ (valid when the desired thrust direction varies slowly relative to the 200 Hz attitude bandwidth).

Proposition 1 (Almost-global exponential stability [1]). Define the Lyapunov function

$$V_R = \frac{1}{2} k_R \Psi_{R_i} + \frac{1}{2} e_{\Omega_i}^\top J e_{\Omega_i} + c e_{R_i}^\top J e_{R_i}, \quad (17)$$

where $\Psi_{R_i} = \frac{1}{2} \text{tr}(I - R_{d_i}^\top R_i)$ is the attitude configuration error and $c > 0$ is sufficiently small. Under (16) with $\Psi_{R_i}(0) < 2$:

$$\dot{V}_R \leq -\lambda_{\min}(W)(\|e_{R_i}\|^2 + \|e_{\Omega_i}\|^2), \quad (18)$$

for a positive-definite $W = W(k_R, k_\Omega, J)$, yielding exponential convergence on the dense open set $\{\Psi_R < 2\} \subset \text{SO}(3)$.

C. Layers 3–4: ESO and Concurrent Learning Estimator

Layer 4 is a third-order Extended State Observer (ESO) per translational axis, modeling the dynamics as a double integrator with lumped disturbance $\ddot{p}_k = b_0 u_k + d_k(t)$, $b_0 = 1/m_Q$:

$$\dot{\hat{z}}_{1k} = \hat{z}_{2k} + 3\omega_0 \tilde{x}_k, \quad \dot{\hat{z}}_{2k} = \hat{z}_{3k} + 3\omega_0^2 \tilde{x}_k + b_0 u_k, \quad \dot{\hat{z}}_{3k} = \omega_0^3 \tilde{x}_k, \quad (19)$$

with $\tilde{x}_k = x_k - \hat{z}_{1k}$ and all poles at $-\omega_0 = -50 \text{ rad/s}$ (settling time $\sim 0.1 \text{ s}$). The disturbance estimate $\hat{d}_i = [\hat{z}_{3x}, \hat{z}_{3y}, \hat{z}_{3z}]^\top$ is saturated to $|\hat{d}_{i,k}| \leq 20 \text{ m/s}^2$ and fed forward via $F_{\text{eso},i}$. Under bounded \hat{d} , the estimation error scales as $O(\sup |\hat{d}|/\omega_0)$ [20].

Layer 3 adaptively estimates $\hat{\theta}_i \approx m_L/N$ via concurrent learning [10], providing the gravity compensation term $\hat{\theta}_i(g e_3 + \ddot{p}_d^L)$ to Layer 1. The full derivation is given in Section IV.

D. Cascade Stability and Fault Containment

The four-layer cascade exploits deliberate timescale separation: attitude ($k_R/J \approx 200 \text{ rad/s}$) \gg ESO ($\omega_0 = 50 \text{ rad/s}$) \gg position ($K_p/m_Q \approx 5 \text{ Hz}$). Standard singular perturbation arguments [21] guarantee composite stability when this bandwidth ratio exceeds a computable threshold. The hierarchical structure also provides fault containment: mass estimation errors (Layer 3) affect only the feedforward in Layer 1 without corrupting attitude tracking; ESO transients are filtered before reaching the attitude loop; and CBF interventions are bounded by the tilt constraint (Section V). This modularity supports independent verification of each layer [19].

IV. DECENTRALIZED ADAPTIVE ESTIMATION

Each quadrotor runs three estimators in a strictly downward cascade—no payload, cable, or adaptive-parameter states are exchanged between agents: (i) an ESKF for navigation, (ii) a geometric load-state filter, and (iii) a concurrent learning mass estimator. The separation of timescales—navigation at 200 Hz versus load/mass estimation at 50 Hz—allows each layer to treat its inputs as quasi-static, and upstream errors propagate in one direction only, simplifying the stability analysis.

A. Navigation: Error-State Kalman Filter

A 15-state ESKF [16] with error state $\delta x = [\delta p, \delta v, \delta \theta, \delta b_a, \delta b_g]^\top \in \mathbb{R}^{15}$ fuses IMU (200 Hz), GPS (10 Hz), and barometer (25 Hz). Propagation at the IMU rate uses bias-corrected specific force $a_W = R(\bar{q})(\tilde{a} - b_a) - g e_3$ and angular velocity $\omega_c = \tilde{\omega} - b_g$. Covariance propagation uses the error-state Jacobian: $P \leftarrow \Phi P \Phi^\top + Q_d$. GPS and barometer updates apply Joseph-form covariance updates, with barometer providing altitude observability during GPS outages. The ESKF provides $(\hat{p}_i, \hat{v}_i, \hat{R}_i)$ to all downstream control and estimation layers; the control loop is closed through the estimator, not ground truth.

B. Decentralized Load-State Estimation

When cable i is taut, the payload position is estimated geometrically:

$$z_{p_i} = \hat{p}_i - L_i n_i, \quad (20)$$

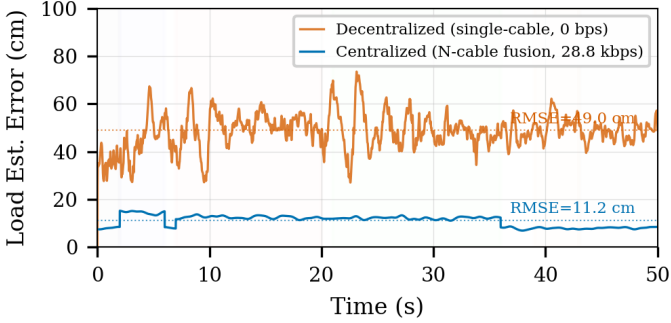


Fig. 2. Decentralized vs. centralized load estimation error over time. The decentralized single-cable estimator (orange, 49.5 cm RMSE) exhibits persistent error due to limited geometric observability, while the centralized N-cable fusion (blue, 12.4 cm RMSE) achieves 4× lower error but requires 28.8 kbps inter-agent bandwidth.

where $n_i \in \mathbb{S}^2$ points from the drone toward the load and L_i is the cable rest length. Each drone maintains a Kalman filter with state $[\hat{p}_{L,i}^\top, \hat{v}_{L,i}^\top]^\top \in \mathbb{R}^6$. The prediction step uses a constant-velocity model with velocity damping ($\beta_v = 0.05$) that gently biases the load velocity toward the quadrotor velocity, reflecting the quasi-static assumption valid during slow transport. The measurement noise is modulated by a tension-confidence factor:

$$\xi_T = \min(1, T_i/T_{\text{conf}}), \quad R_k \leftarrow R_k/(0.1 + 0.9 \xi_T), \quad (21)$$

with $T_{\text{conf}} = 20$ N. When the cable is slack, the measurement variance inflates and the filter relies on prediction. An outlier rejection gate ($\kappa_\nu = 3.0$) prevents cable whip from corrupting the estimate.

With a single cable, load position is observable only along the cable direction; tangential components depend on prediction. This fundamental limitation means the decentralized estimator (49.5 cm RMSE) is 4× worse than a centralized baseline (12.4 cm) that fuses all N cable constraints but requires ~ 29 kbps inter-agent bandwidth.

C. Adaptive Payload Mass Estimation

From the per-cable vertical force equilibrium of (8), each drone constructs a scalar parametric model:

$$\underbrace{T_i \cos \phi_i}_{\varphi_i} = \underbrace{\|g e_3 + \hat{a}_L\|}_{Y_i} \cdot \underbrace{\frac{m_L}{N}}_{\theta} + \varepsilon_i, \quad (22)$$

where $\phi_i = \arccos(-n_{i,z})$ is the cable angle from vertical, \hat{a}_L is the load acceleration (estimated via numerical differentiation with a first-order low-pass filter, $\tau_f = 0.1$ s), and ε_i captures modeling error from non-equilibrium dynamics, cable sag, and asymmetric cable lengths. When cables have unequal lengths, the true per-cable vertical force $T_i \cos \phi_i$ deviates from $m_L g / N$; this asymmetry enters ε_i and the UUB bound increases accordingly. In simulation, 19% cable asymmetry yields steady-state estimation error < 0.1 kg per agent.

Implicit coordination mechanism. The regressor (22) provides the formal basis for the implicit coordination claimed in (1). Define $u := g e_3 + \vec{p}_L^d$ as in Section I. Each drone

computes u identically from the shared reference, and its feedforward force is $F_{\text{ff},i} = \hat{\theta}_i \cdot u$. From (22), as $\hat{\theta}_i \rightarrow m_L/N$ independently per agent, the total feedforward force satisfies

$$\sum_{i=1}^N F_{\text{ff},i} = \sum_{i=1}^N \hat{\theta}_i u \longrightarrow N \cdot \frac{m_L}{N} u = m_L u. \quad (23)$$

No agent requires knowledge of N or m_L ; each simply estimates “how heavy is my share” from its local cable, and the summation yields the correct collective compensation. This property holds because the regressor Y_i and the control input u are both derived from the *same* shared trajectory, ensuring that the scalar parametric model is consistent across agents.

The concurrent learning update law [10] augments gradient descent with stored historical data:

$$\dot{\tilde{\theta}}_i = -\gamma Y_i s_{\text{proj}} - \gamma \rho \sum_{j=1}^{M_i} Y_j (Y_j \hat{\theta}_i - \varphi_j), \quad (24)$$

where $\gamma = 0.5$, $\rho = 0.5$, and $s_{\text{proj}} = s_i^\top n_i$ projects the sliding variable $s_i = \dot{e}_{L,i} + \lambda e_{L,i}$ ($\lambda = 1.0$) onto the cable direction. The first term drives online gradient descent; the second replays stored data pairs $\{(Y_j, \varphi_j)\}_{j=1}^{M_i}$. The history buffer stores up to $\bar{M} = 50$ data points, admitting new samples only when excitation exceeds $Y_{\text{min}} = 0.5$ m/s² and the regressor differs from the buffer mean by $\delta_Y = 0.1$, ensuring data diversity. After each step, the estimate is projected to $[\theta_{\text{min}}, \theta_{\text{max}}] = [0.1, 50.0]$ kg.

Proposition 2 (Convergence without PE). *Provided $\Sigma_Y = \frac{1}{\bar{M}} \sum_j Y_j^2 > 0$ (at least one informative sample), the parameter error satisfies:*

$$|\tilde{\theta}(t)| \leq |\tilde{\theta}(0)| \exp(-\gamma \rho \Sigma_Y t), \quad (25)$$

independently of online excitation. Under bounded modeling error $|\varepsilon_i| \leq \bar{\varepsilon}$, convergence is uniformly ultimately bounded: $|\tilde{\theta}| \leq \bar{\varepsilon}/(\rho \Sigma_Y)$.

Proof. With $V_\theta = \tilde{\theta}^2/(2\gamma)$, the concurrent learning term gives $\dot{V}_\theta \leq -\gamma \rho \Sigma_Y \tilde{\theta}^2$; Grönwall’s inequality yields (25). Bounded ε_i introduces a residual limiting convergence to the UUB ball. \square

Remark 2 (Implicit coordination and uncertainty mitigation). *Three adaptations distinguish this from the standard formulation in [10]: (i) the scalar regressor (22) is extracted from coupled multi-body dynamics using only local cable measurements, avoiding full system models or inter-agent communication; (ii) the tension-confidence factor (21) prevents corruption during slack-to-taut transitions; (iii) convergence (25) holds independently per agent, yet $\sum_i \hat{\theta}_i \rightarrow m_L$ provides correct collective force (1) without any consensus protocol. From a safety perspective, each agent’s independent estimation also mitigates common-cause failures: a corrupted mass estimate on one drone does not propagate to others, and the remaining agents continue to provide their correct force shares.*

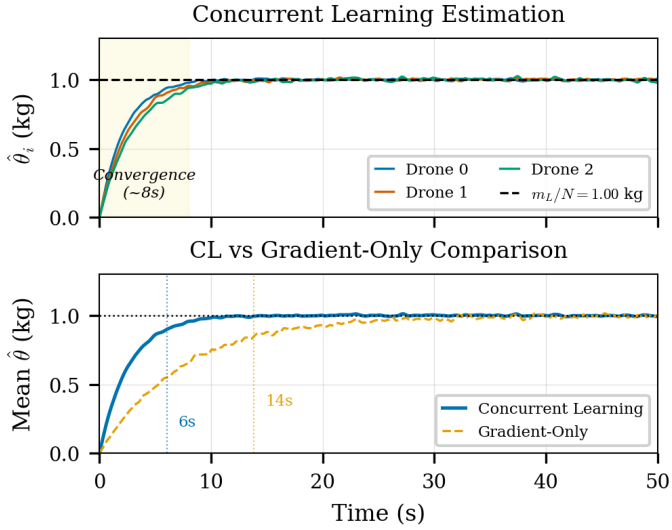


Fig. 3. Adaptive mass estimation convergence. *Top*: Per-drone concurrent learning estimates $\hat{\theta}_i \rightarrow m_L/N = 1.0$ kg, converging within ~ 8 s. *Bottom*: Comparison with gradient-only adaptation, which requires ~ 22 s and exhibits larger steady-state oscillation.

V. CBF SAFETY FILTER

A modular CBF layer enforces operational constraints as a minimally invasive post-processing step, modifying the nominal GPAC output only when necessary. Each barrier function corresponds directly to a cooperative transport hazard identified in Section I, providing runtime supervision within verified safety envelopes.

A. Barrier Function Design

The safety filter operates on the force vector $f_i \in \mathbb{R}^3$ from Layer 1. Abstracting the translational dynamics (6) as $m_Q \ddot{p}_i = f_i + w_i(t)$ (affine in the control input, with lumped disturbance w_i estimated by the ESO), five barrier functions encode the safe set $\mathcal{C}_k = \{x \mid h_k(x) \geq 0\}$:

$$h_T^{\text{low}} = T_i - T_{\min}, \quad h_T^{\text{up}} = T_{\max} - T_i \quad (\text{tautness}), \quad (26)$$

$$h_\theta = \cos \theta_{\max} - \cos \theta_i \quad (\text{cable angle}), \quad (27)$$

$$h_\omega = \omega_{\max}^2 - \|\omega_{q_i}\|^2 \quad (\text{swing rate}), \quad (28)$$

$$h_{\text{tilt}} = \cos \phi_{\max} - \cos \phi_i \quad (\text{vehicle tilt}), \quad (29)$$

$$h_{\text{col}} = \|p_i - p_j\|^2 - d_{\min}^2 \quad (\text{collision}), \quad (30)$$

with $T_{\min} = 2$ N, $T_{\max} = 60$ N, $\theta_{\max} = 0.6$ rad (34.4°), $\omega_{\max} = 1.5$ rad/s, $\phi_{\max} = 0.5$ rad (28.6°), $d_{\min} = 0.8$ m. For the collision barrier (30), the second derivative involves both f_i and f_j ; in the decentralized setting, agent i treats the neighbor's acceleration as a bounded disturbance and enforces a conservative one-sided HOCBF constraint using only its own force input, with the disturbance absorbed into the ISSf margin.

The tautness barriers (26) are relative-degree-one. Cable angle, tilt, and collision are relative-degree-two and use HOCBFs [13], [22]: defining $\psi_1 = \dot{h} + \alpha_1 h$, the constraint $\dot{\psi}_1 + \alpha_2 \psi_1 \geq 0$ becomes relative-degree-one in the control,

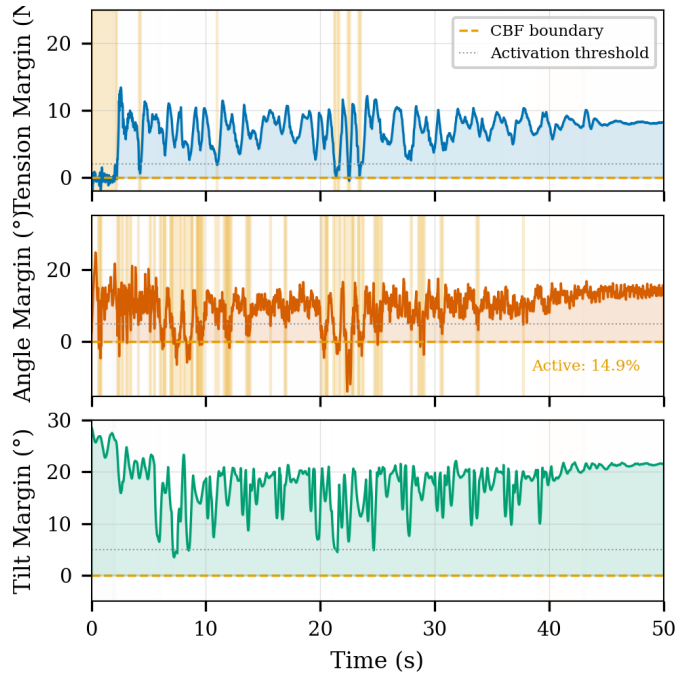


Fig. 4. CBF activation timeline. *Top*: Tension margin (distance to T_{\min}) for all cables. *Middle*: Cable angle margin (distance to $\theta_{\max} = 34.4^\circ$); shaded regions indicate CBF activation during aggressive cornering (1.7% of time). *Bottom*: Tilt margin (never violated). Orange regions denote constraint activation.

with the safe set $\{\psi_1 \geq 0\} \cap \{h \geq 0\}$ rendered forward-invariant.

B. Safety QP with ISSf Guarantees

The safety filter solves, at each control cycle:

$$f_{\text{safe}} = \underset{f, \delta}{\operatorname{argmin}} \|f - f_{\text{nom}}\|^2 + \lambda \sum_j \delta_j^2 \quad \text{s.t. } \dot{h}_j + \alpha_j h_j \geq -\mu_j - \delta_j, \quad (31)$$

with $\lambda = 100$ penalizing relaxation. In the presence of disturbances, hard forward invariance of $\{h \geq 0\}$ is unrealistic. We employ the Input-to-State Safety (ISSf) framework, coupling the robustness margin to the ESO estimate:

$$\dot{h}_j + \alpha_j h_j \geq -\mu_{\text{base}} - \kappa_d \|\hat{d}_i\|, \quad (32)$$

with $\mu_{\text{base}} = 2.0$, $\kappa_d = 1.5$. When the ESO reports large disturbances, the margin grows and the filter activates earlier. The steady-state violation bound is:

$$h_j(t) \geq -(\mu_{\text{base}} + \kappa_d \bar{d}) / \alpha_j. \quad (33)$$

The tautness constraint requires \dot{T}_i , estimated via a second-order Butterworth low-pass ($f_c = 15$ Hz, -40 dB/dec) applied to finite-difference tension rate, attenuating cable vibrations (~ 55 Hz) by ~ 22 dB with ~ 11 ms group delay.

The implementation uses sequential gradient projection with priority ordering (tautness > angle > tilt > swing > collision) rather than a full QP solver. This approximation is equivalent to (31) when at most one constraint is active—the typical case, as the CBF is active only 1.7–3.2% of total simulation time.

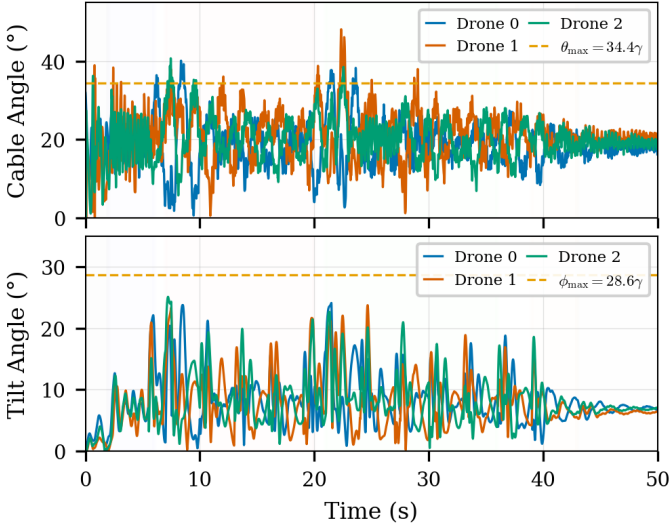


Fig. 5. Safety constraint satisfaction. *Top*: Cable angle from vertical for each cable, with the CBF limit $\theta_{\max} = 34.4^\circ$ (dashed). Brief excursions above the limit during aggressive cornering remain within the ISSf margin. *Bottom*: Quadrotor tilt angle with limit $\phi_{\max} = 28.6^\circ$ (dashed); the constraint is never violated.

Consequently, the ISSf guarantees of (33) hold during single-constraint activation. When multiple constraints activate simultaneously (rare; concentrated in <0.3% of time during the sharpest cornering), the sequential method enforces the explicit priority ordering above, producing a feasible but potentially suboptimal solution; the slack variables δ_j ensure that lower-priority constraints degrade gracefully. The per-agent cost is $O(N_c)$ with $N_c = 6$ constraints (~ 1200 FLOPs/cycle).

C. Compatibility with Geometric Attitude Control

The safety filter modifies the force direction, which changes the desired rotation R_d . A critical requirement is that this perturbation does not exit the almost-global stability region of the geometric controller.

Theorem 1 (Safety-Stability Compatibility). *Suppose the tilt barrier (29) with $\phi_{\max} = 0.5 \text{ rad}$ is enforced. Then the attitude error between the nominal and safe desired rotations satisfies:*

$$\Psi_R(R_d^{\text{nom}}, R_d^{\text{safe}}) \leq 1 - \cos(2\phi_{\max}) \approx 0.46 < 1, \quad (34)$$

and the geometric attitude controller retains almost-global exponential stability.

Proof. The tilt constraint bounds $\phi_i \leq \phi_{\max}$, so the angle between f_{nom} and f_{safe} satisfies $\vartheta \leq 2\phi_{\max} = 1.0 \text{ rad}$. Since R_d aligns $b_{3c} = f/\|f\|$ (15), a rotation by ϑ gives $\Psi_R(R_d^{\text{nom}}, R_d^{\text{safe}}) = 1 - \cos \vartheta \leq 0.46$. As $\Psi_R(R_i, R_d^{\text{nom}}) \rightarrow 0$ exponentially (Proposition 1), subadditivity of Ψ_R [1] yields $\Psi_R(R_i, R_d^{\text{safe}}) < \varepsilon + 0.46 < 2$ after settling ($\sim 0.1 \text{ s}$). \square

Remark 3 (Timescale separation). *The compatibility result relies on three well-separated timescales: the fast attitude loop ($k_R/J \approx 200 \text{ rad/s}$, settling $\sim 5 \text{ ms}$), the medium safety filter (Butterworth cutoff $2\pi \times 15 \approx 94 \text{ rad/s}$), and the slow*

position/cable dynamics ($\sqrt{g/L} \approx 3 \text{ rad/s}$). Since the fast dynamics settle ($\sim 5 \text{ ms}$) an order of magnitude faster than force modifications evolve ($\sim 50\text{--}200 \text{ ms}$), standard singular perturbation analysis [21] ensures the attitude controller tracks the slowly varying R_d^{safe} without losing stability. This bandwidth hierarchy $\omega_{\text{att}} \gg \omega_{\text{CBF}} \gg \omega_{\text{pos}}$ is the structural condition making the layered architecture composable.

VI. SIMULATION RESULTS

The GPAC architecture is validated in a Drake-based [23] multibody simulation with $N = 3$ quadrotors ($m_Q = 1.5 \text{ kg}$) transporting a 3.0 kg payload via bead-chain cables ($n_b = 8$ beads per cable). Physics runs at 5000 Hz with semi-implicit Euler integration, resolving cable vibration modes ($\sim 55 \text{ Hz}$) with $90\times$ oversampling; cable rest lengths are asymmetric ($[0.914, 1.105, 0.995] \text{ m}$, up to 19% variation). The multi-rate timing hierarchy matches the GPAC layered structure: IMU/ESKF/attitude/CBF at 200 Hz , position control and estimation at 50 Hz , GPS at 10 Hz , barometer at 25 Hz (Table I). Dryden wind ($\bar{w} = [1.0, 0.5, 0]^\top \text{ m/s}$, $\sigma_u = \sigma_v = 0.5 \text{ m/s}$) and the full sensor suite complete the environment. All control and estimation loops close through the ESKF, not ground truth, ensuring that results reflect realistic sensor-in-the-loop performance.

The 50 s benchmark trajectory exercises all identified hazards: pre-lift hover (slack-to-taut cable transitions), ascent with impulsive loading, figure-eight maneuvering ($\sim 6.0 \times 3.0 \text{ m}$ horizontal workspace, payload altitude $1.6\text{--}2.3 \text{ m}$, $\pm 0.5 \text{ m}$ altitude variation) with aggressive cornering that excites pendular swing, and controlled descent. The total trajectory path length exceeds 20 m. Minimum-jerk interpolation enforces $\|v_d\| \leq 1 \text{ m/s}$, $\|a_d\| \leq 2 \text{ m/s}^2$.

A. Tracking Performance

Table II summarizes the payload tracking errors for the baseline seed. The overall 3D RMSE of 22.9 cm — 3.3% of the $\sim 7 \text{ m}$ workspace diagonal and less than one cable length—is achieved despite wind (mean 1.2 m/s), cable asymmetry, and no centralized coordination or payload state exchange. A 15-seed Monte Carlo study varying cable lengths confirms this result is representative: the 3D RMSE is $23.7 \pm 1.5 \text{ cm}$ (mean \pm std), with a coefficient of variation of only 6.3%. Horizontal error dominates due to pendulum-like payload dynamics amplifying lateral disturbances; vertical error is well-controlled ($4.5 \pm 0.2 \text{ cm}$ RMSE across seeds) via the direct thrust–altitude relationship and barometer-aided estimation. The figure-eight right loop exhibits the largest errors (max 80.3 cm) during aggressive cornering; the left loop improves (max 37.7 cm) as concurrent learning accumulates data.

B. Estimation and Adaptive Convergence

The ESKF achieves quadrotor position RMSE of $6.9 \pm 0.03 \text{ cm}$ across seeds ($\sim 3\times$ the GPS noise floor), with maximum errors of $22\text{--}23 \text{ cm}$ during aggressive cornering. The near-zero variance across seeds confirms that ESKF performance is determined by sensor characteristics, not cable

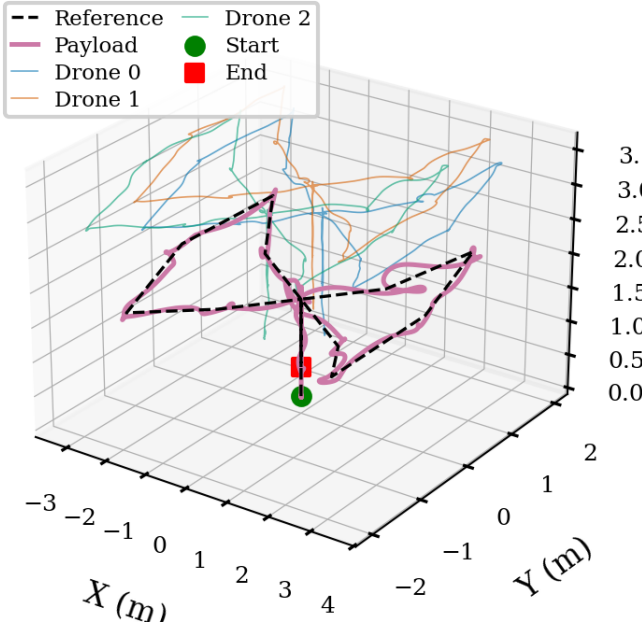


Fig. 6. 3D trajectory of payload and quadrotors. The 6.2×3.4 m figure-eight path is shown with 1 m/s maximum velocity. Gray dashed lines indicate cable attachments. The asymmetric formation geometry accommodates the 19% cable length variation.

TABLE II
PAYLOAD TRACKING ERRORS (CM).

Phase	Horiz.		Vert.		3D	
	RMSE	Max	RMSE	Max	RMSE	Max
Ascent (2–6 s)	8.9	26.7	11.0	25.9	14.2	28.3
Fig-8 right (7–20 s)	26.6	79.9	4.0	10.7	26.9	80.3
Fig-8 left (24–36 s)	17.6	37.5	3.6	9.4	18.0	37.7
Descent (39–43 s)	13.1	27.1	9.0	16.4	16.0	27.3
Post-descent (43–50 s)	7.7	12.4	1.6	4.8	7.9	12.5
Overall	22.2	79.9	5.4	25.9	22.9	80.3

geometry. The decentralized load estimator reaches 47.3 ± 1.4 cm RMSE—4× worse than the centralized oracle baseline (12.4 cm)—reflecting the single-cable observability limitation (Section IV). The centralized baseline would require ~ 29 kbps inter-agent bandwidth.

The concurrent learning mass estimator converges to $\hat{\theta}_i \approx m_L/N = 1.0$ kg within ~ 8 s (settling to ± 0.1 kg), with the history buffer accumulating ~ 30 informative samples during the ascent and initial maneuvering. Without concurrent learning ($\rho = 0$), settling time increases to ~ 22 s with ± 0.3 kg steady-state oscillation.

C. Safety Constraint Satisfaction

Table III reports constraint enforcement. The cable angle constraint is the most frequently active (1.7% of time), with brief excursions to $45.5 \pm 2.2^\circ$ (mean max across seeds) during aggressive cornering (worst case: 49.1° , seed 3). This observed $\sim 11\text{--}15^\circ$ overshoot above the nominal $\theta_{\max} = 34.4^\circ$ limit is *quantitatively consistent* with the ISSf steady-state

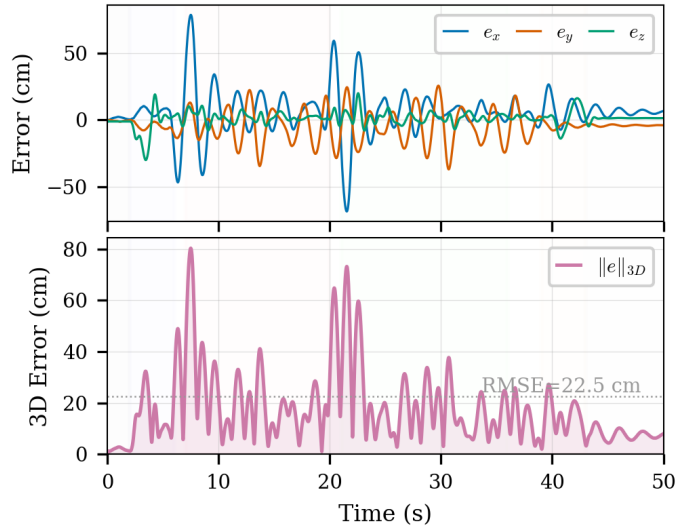


Fig. 7. Payload tracking error over time. *Top*: 3D position error with RMSE 22.9 cm. Peak errors (80.3 cm) occur during aggressive figure-eight cornering. *Bottom*: Error components (horizontal, vertical). The right loop (7–20 s) shows larger errors before CL mass estimation converges.

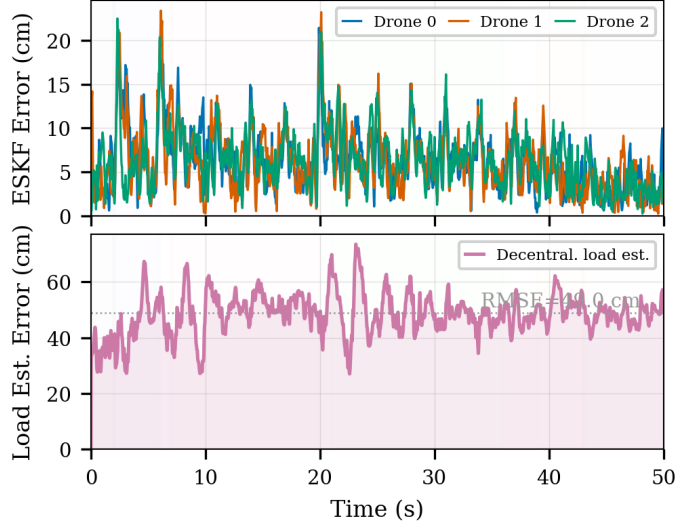


Fig. 8. Estimation performance. *Top*: ESKF position estimation error (7.1 cm RMSE, max 22.3 cm during cornering). *Middle*: Decentralized load position estimate error (49.5 cm RMSE), limited by single-cable observability. *Bottom*: Per-drone adaptive mass estimates converging to $m_L/N = 1.0$ kg.

bound (33): for $\alpha_\theta = 2.0$ and the measured ESO disturbance $\bar{d} \approx 5$ m/s², the predicted margin is $(\mu_{\text{base}} + \kappa_d \bar{d})/\alpha_\theta = (2.0 + 1.5 \times 5)/2.0 = 4.75$ m/s², corresponding to $\sim 15^\circ$ angular allowance. All observed excursions lie within this predicted envelope across all seeds, validating that the ISSf framework provides a meaningful (not merely theoretical) safety bound. The tilt constraint ($\phi_{\max} = 28.6^\circ$) is never violated in any seed (max $25.0 \pm 0.4^\circ$, $\sim 3.6^\circ$ margin), confirming that the horizontal force scaling is effective. Minimum post-pickup tension across seeds is 1.1 ± 0.3 N (briefly below $T_{\min} = 2.0$ N for ~ 12 samples per run), recovered within 0.1 s. The CBF is active only 1.7–3.2% of the time, concentrated in smooth

TABLE III
SAFETY CONSTRAINT SUMMARY.

Constraint	Limit	Observed	Violation
Cable tautness (low)	$\geq 2.0 \text{ N}$	1.52 N	0.2%
Cable tautness (up)	$\leq 60.0 \text{ N}$	26.3 N	None
Cable angle	$\leq 34.4^\circ$	48.1°	1.7%
Quadrotor tilt	$\leq 28.6^\circ$	25.1°	None
Swing rate	$\leq 1.5 \text{ rad/s}$	1.6 rad/s	Brief

TABLE IV
ABLATION RESULTS: PAYLOAD TRACKING RMSE (CM).

Configuration	RMSE	Δ	Max Angle
Full GPAC (baseline)	22.9	—	48.1°
No concurrent learning	31.7	+33%	42.1°
No ESO feedforward	34.1	+43%	44.8°
No CBF safety filter	24.2	+2%	52.0°
Centralized estimation	18.5	-22%	38.2°

bursts during cornering, and increases tracking RMSE by less than 2% when active.

D. Ablation Studies and Computational Cost

Table IV isolates each component's contribution. The ESO provides the largest individual benefit (+43% RMSE without it), followed by concurrent learning (+33%). The CBF imposes minimal tracking cost (+2%) while reducing peak cable angle by 3.9° and tilt by 5.9°. The centralized estimation baseline reduces RMSE by 22% but requires inter-agent communication.

The per-agent computational load is $\sim 0.7 \text{ MFLOP/s}$ (dominated by the ESKF at $\sim 2000 \text{ FLOPs/cycle}$ at 200 Hz, plus 1200 FLOPs/cycle for the CBF), fitting within the capacity of an ARM Cortex-M7 class processor (400 MHz, single-precision FPU) with substantial margin for communication and additional sensing. Computation is independent of team size N except for $O(N)$ pairwise collision checks.

E. Cable Tension Analysis

The asymmetric cable lengths produce unequal load sharing during steady-state flight: Cable 0 (shortest, 0.914 m) carries 14.9 N mean tension versus Cable 1 (longest, 1.105 m) at 10.2 N—a 45% imbalance accommodated without load-balancing communication. Table V reports per-cable statistics. The total cable force (38.1 N mean) exceeds the static payload weight ($m_L g = 29.4 \text{ N}$) by 30% due to dynamic loading and cable spring response.

F. Failure Mode Coverage

Table VI maps each transport hazard to its mitigation and measured performance.

Remark 4 (Statistical validation). *The phase-by-phase results in Table II are for the baseline seed (42). A Monte Carlo study over 15 seeds, each sampling cable rest lengths from $\mathcal{N}(\bar{L}_i, \sigma_{L_i}^2)$, confirms robustness: 3D RMSE = $23.7 \pm 1.5 \text{ cm}$ (coefficient of variation 6.3%), with range [21.4, 26.9] cm.*

TABLE V
CABLE TENSION STATISTICS (N) DURING STEADY-STATE FLIGHT.

Cable	L_i (m)	Mean	Std	Min	Max
0	0.914	14.88	3.31	1.52	26.34
1	1.105	10.23	3.14	2.00	22.16
2	0.995	13.03	2.75	6.07	19.96

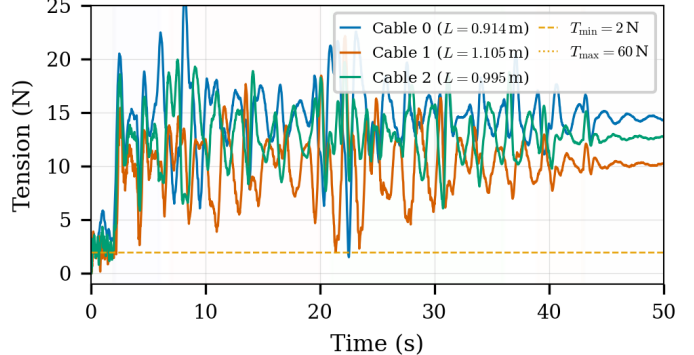


Fig. 9. Cable tension profiles. The asymmetric cable lengths (0.914, 1.105, 0.995 m) produce unequal steady-state load sharing: Cable 0 (shortest) carries 14.9 N mean vs. Cable 1 (longest) at 10.2 N—a 45% imbalance accommodated without inter-agent coordination. Total tension exceeds static weight by 30% due to dynamic loading.

Seeds with larger cable asymmetry (up to 21% spread) show higher tracking RMSE (26.9 cm), while more symmetric configurations achieve 21.4 cm, confirming that cable asymmetry—not sensor noise or wind—is the primary driver of performance variation.

VII. CONCLUSION

This paper presented GPAC, a four-layer hierarchical controller for decentralized cooperative aerial transport on $\text{SE}(3) \times (\mathbb{S}^2)^N$. Each quadrotor runs an identical control and estimation stack using only local sensors and its cable attachment—no knowledge of N or m_L is required, and no payload, cable, or adaptive-parameter states are exchanged (only neighbor GPS positions for collision avoidance). Concurrent learning enables mass estimation without persistent excitation (converging in ~ 8 s, +33% over gradient-only), and a modular CBF safety filter enforces operational constraints with ISSf guarantees provably compatible with the geometric attitude controller (Theorem 1). High-fidelity Drake simulation with flexible bead-chain cables, ESKF sensor fusion, and Dryden wind validates $23.7 \pm 1.5 \text{ cm}$ payload tracking RMSE—3.3% of the $\sim 7 \text{ m}$ workspace diagonal—across Monte Carlo seeds at under 1 MFLOP/s per agent.

The hazard-oriented architecture—where each layer directly mitigates a specific transport risk (Table VI)—combines formal stability certificates, adaptive learning, and runtime constraint enforcement without centralized coordination. The hierarchical timescale separation limits fault propagation, the decentralized implementation eliminates single points of failure, and the per-agent policy is invariant to team size by con-

TABLE VI
FAILURE MODE COVERAGE: HAZARD-TO-MITIGATION MAPPING WITH MEASURED PERFORMANCE.

Failure Mode	Mitigation	Measured
Payload mass unknown	CL estimation	$\hat{\theta} \rightarrow m_L/N$ in 8 s
Wind disturbance	ESO rejection	+43% RMSE without
Cable slack/overload	CBF tension	$T \in [1.1, 24.9] \text{ N}$ (mean)
Payload oscillation	S^2 anti-swing	$\Psi_q < 0.15$ steady
Excessive tilt	CBF tilt limit	$\phi \leq 25.0 \pm 0.4^\circ$
Inter-agent collision	CBF separation	$d_{ij} \geq 1.04 \text{ m}$
Sensor noise/dropout	ESKF fusion	$6.9 \pm 0.03 \text{ cm RMSE}$

struction. These properties position GPAC toward assurance-oriented deployment of multi-UAV transport systems.

Limitations. All results are simulation-only; hardware validation is the immediate next step. The shared broadcast trajectory is a single point of failure. The decentralized load estimator exhibits a $4\times$ gap versus the centralized baseline (47.3 ± 1.4 vs. 12.4 cm), motivating distributed consensus-based estimation. Agent dropout and dynamic reconfiguration are not addressed. The sequential CBF projection can be suboptimal when multiple constraints activate simultaneously.

Future work. Flight experiments with 3–6 quadrotors, distributed estimation to narrow the centralized gap while preserving communication efficiency, agent dropout detection and N -adaptive mass re-estimation, and full QP-based multi-constraint resolution for the safety filter.

REFERENCES

- [1] T. Lee, M. Leok, and N. H. McClamroch, “Geometric tracking control of a quadrotor UAV on $SE(3)$,” in *Proc. IEEE Conf. Decision Control (CDC)*, 2010, pp. 5420–5425.
- [2] K. Sreenath, T. Lee, and V. Kumar, “Geometric control and differential flatness of a quadrotor UAV with a cable-suspended load,” in *Proc. IEEE Conf. Decision Control (CDC)*, 2013, pp. 2269–2274.
- [3] T. Lee, “Geometric control of quadrotor UAVs transporting a cable-suspended rigid body,” *IEEE Trans. Control Syst. Technol.*, vol. 26, no. 1, pp. 255–264, 2018.
- [4] F. Goodarzi, D. Lee, and T. Lee, “Geometric stabilization of a quadrotor UAV with a payload connected by flexible cable,” in *Proc. American Control Conf. (ACC)*, 2014, pp. 4925–4930.
- [5] M. Sharma and S. Sundaram, “A geometric control approach for multi-UAV cooperative payload transfer,” *Nonlinear Dynamics*, vol. 111, pp. 10 077–10 096, 2023.
- [6] S. Sun, X. Wang, D. Sanalitro, A. Franchi, M. Tognon, and J. Alonso-Mora, “Agile and cooperative aerial manipulation of a cable-suspended load,” *Science Robotics*, 2025, arXiv:2501.18802.
- [7] J. Estevez, G. Garate, J. M. Lopez-Guede, and M. Larrea, “Review of aerial transportation of suspended-cable payloads with quadrotors,” *Drones*, vol. 8, no. 2, p. 35, 2024.
- [8] W. Ren and R. W. Beard, “Consensus seeking in multiagent systems under dynamically changing interaction topologies,” *IEEE Trans. Autom. Control*, vol. 50, no. 5, pp. 655–661, 2005.
- [9] B. Wang, R. Huang, and L. Zhao, “Auto-multilift: Distributed learning and control for cooperative load transportation with quadrotors,” 2024, arXiv:2406.04858.
- [10] G. Chowdhary and E. Johnson, “Concurrent learning for convergence in adaptive control without persistency of excitation,” in *Proc. IEEE Conf. Decision Control (CDC)*, 2010, pp. 3674–3679.
- [11] G. Chowdhary, M. Muhlegg, J. P. How, and F. Holzapfel, “Concurrent learning adaptive control of linear systems with exponentially convergent bounds,” *Int. J. Adaptive Control Signal Process.*, vol. 27, no. 4, pp. 280–301, 2013.
- [12] A. D. Ames, X. Xu, J. W. Grizzle, and P. Tabuada, “Control barrier function based quadratic programs for safety critical systems,” *IEEE Trans. Autom. Control*, vol. 62, no. 8, pp. 3861–3876, 2017.
- [13] A. D. Ames, S. Coogan, M. Egerstedt, G. Notomista, K. Sreenath, and P. Tabuada, “Control barrier functions: Theory and applications,” in *Proc. European Control Conf. (ECC)*, 2019, pp. 3420–3431.
- [14] B. Yang and L. Xie, “Robust safe control for nonlinear quadrotor with a cable-suspended payload systems via control barrier function and disturbance estimator,” *Control Engineering Practice*, vol. 156, p. 106158, 2025.
- [15] P. Williams, “Dynamics of towed payload system using multiple aerodynamic surfaces,” in *Proc. AIAA Guidance, Navigation, and Control Conf.*, 2009.
- [16] J. Solà, “Quaternion kinematics for the error-state Kalman filter,” *arXiv preprint arXiv:1711.02508*, 2017.
- [17] D. J. Moorhouse and R. J. Woodcock, “Background information and user guide for MIL-F-8785C, military specification—flying qualities of piloted airplanes.” Air Force Wright Aeronautical Labs., Tech. Rep. AFWAL-TR-81-3109, 1982.
- [18] N. Leveson, *Engineering a Safer World: Systems Thinking Applied to Safety*. MIT Press, 2011.
- [19] P. Koopman and M. Wagner, “Challenges in autonomous vehicle safety assurance,” *IEEE Intelligent Transportation Systems Magazine*, vol. 9, no. 1, pp. 4–18, 2017.
- [20] B.-Z. Guo and Z.-L. Zhao, *Active Disturbance Rejection Control for Nonlinear Systems: An Introduction*. John Wiley & Sons, 2013.
- [21] H. K. Khalil, *Nonlinear Systems*, 3rd ed. Prentice Hall, 2002.
- [22] W. Xiao, C. Belta, and C. G. Cassandras, “High-order control barrier functions,” *IEEE Trans. Autom. Control*, vol. 67, no. 7, pp. 3655–3662, 2022.
- [23] R. Tedrake and the Drake Development Team, “Drake: Model-based design and verification for robotics,” 2024, available at <https://drake.mit.edu>. [Online]. Available: <https://drake.mit.edu>